

# Hydrodynamical simulations of the Sunyaev–Zel'dovich effect: the kinetic effect

Antonio C. da Silva,<sup>1</sup> Domingos Barbosa,<sup>2,3</sup> Andrew R. Liddle<sup>1</sup>  
and Peter A. Thomas<sup>1</sup>

<sup>1</sup>*Astronomy Centre, University of Sussex, Brighton BN1 9QJ*

<sup>2</sup>*Astrophysics Group, Lawrence Berkeley Laboratory, 1 Cyclotron Road, Berkeley CA 94710, USA*

<sup>3</sup>*CENTRA, Instituto Superior Técnico, Av. Rovisco Pais, 1049-001 Lisboa Codex, Portugal*

20 October 2018

## ABSTRACT

We use hydrodynamical  $N$ -body simulations to study the kinetic Sunyaev–Zel'dovich effect. We construct sets of maps, one square degree in size, in three different cosmological models. We confirm earlier calculations that on the scales studied the kinetic effect is much smaller than the thermal (except close to the thermal null point), with an rms dispersion smaller by about a factor five in the Rayleigh–Jeans region. We study the redshift dependence of the rms distortion and the pixel distribution at the present epoch. We compute the angular power spectra of the maps, including their redshift dependence, and compare them with the thermal Sunyaev–Zel'dovich effect and with the expected cosmic microwave background anisotropy spectrum as well as with determinations by other authors. We correlate the kinetic effect with the thermal effect both pixel-by-pixel and for identified thermal sources in the maps to assess the extent to which the kinetic effect is enhanced in locations of strong thermal signal.

**Key words:** galaxies: clusters, cosmic microwave background

## 1 INTRODUCTION

The Sunyaev–Zel'dovich (SZ) effect (Sunyaev & Zel'dovich 1972, 1980; for reviews see Rephaeli 1995 and Birkinshaw 1999) is the change in energy experienced by cosmic microwave background photons when they scatter from intervening gas, especially that in galaxy clusters. The dominant version from clusters is the thermal SZ effect, the gain in energy acquired from the thermal motion of the gas which is commonly at a temperature of tens of millions of degrees in clusters. The kinetic SZ effect is the Doppler shift arising from the bulk motion of the gas.

The thermal effect has been quite well studied theoretically, and recently has become a burgeoning area of observational activity with the construction of two-dimensional maps of clusters becoming commonplace (Jones et al. 1993; Myers et al. 1997; Carlstrom et al. 2000). By contrast, less attention has been given to the kinetic effect. It presents a considerable observational challenge, because it is predicted to be much smaller than the thermal effect on the angular scales explored so far, and also because unlike the thermal effect it possesses no characteristic spectral signature allowing it to be distinguished from primary cosmic microwave background anisotropies. It is also more difficult to make semi-analytic calculations. The thermal effect can be obtained fairly directly via the Press–Schechter

(1974) approach; various aspects including number counts, the global CMB distortion, and its impact as secondary anisotropy for CMB measurements at small scales have been extensively studied (Cole & Kaiser 1988; Colafrancesco et al. 1994, 1997; Bartlett & Silk 1994; Barbosa et al. 1996; Eke, Cole & Frenk 1996; Aghanim et al. 1997; Komatsu & Kitayama 1999; Atrio-Barandela & Mücke 1999; Molnar & Birkinshaw 2000; Hernández-Monteagudo, Atrio-Barandela & Mücke 2000). Predictions for the kinetic effect require the simultaneous estimation of both mass and peculiar velocity, and the signal is much less dominated by the gas which happens to be in massive halos. A detailed analytical model has recently been constructed by Valageas, Balbi & Silk (2000) [see also Benson et al. 2000], which computes the effect including inhomogeneities in reionization; this supersedes earlier modelling by Aghanim et al. (1997) where the peculiar velocities were drawn from a gaussian distribution of fixed width.

We recently used large-scale hydrodynamical  $N$ -body simulations to make simulated maps of the thermal effect and analyzed their properties (da Silva et al. 2000; for similar recent work see Refregier et al. 2000a; Seljak, Burwell & Pen 2000; Springel, White & Hernquist 2000). In this paper, we make a detailed analysis of maps of the kinetic effect, made using the same technique. Recently Springel

et al. (2000) used similar simulations to study the angular power spectrum of the kinetic effect in the  $\Lambda$ CDM cosmology, and investigated the influence of non-gravitational heating upon it. In this paper we study three different cosmologies, and investigate a wide range of properties of the resulting maps including the relation between thermal and kinetic distortion.

## 2 THE KINETIC SZ EFFECT

### 2.1 Linear and non-linear effects

Traditionally, the phrase “kinetic SZ effect” is associated with the scattering of photons from galaxy clusters or other large gravitationally-bound objects. However, in simulations there is no clear distinction between this and the scattering from any other moving gas, and when we construct maps they will be based on the bulk motions of all the material in the simulation box. However, one should recognize that part of this signal is computable in linear perturbation theory, and is for example computed in a run of the CMBFAST program (Seljak & Zaldarriaga 1996) for a cosmology with reionization, where it is called the low-redshift Doppler effect. These different regimes, and their relation to the Ostriker–Vishniac effect (Ostriker & Vishniac 1986), have been discussed in detail by Hu (2000) and by Gnedin & Jaffe (2000), and observational aspects are described by Cooray & Hu (2000).

Concerning the contribution from non-linear evolution, one should recognize that while there are non-linear contributions to the velocities, of particular importance is the non-linear evolution of the density field. This concentrates the matter into a virialized region which gives a high optical depth probe of the bulk velocity at that point. The non-linear effect is more important at low redshifts.

### 2.2 The reionization epoch

Photons only scatter at epochs where the gas is ionized. Reionization is thought to be induced by radiation from the first generation of massive stars in dwarf galaxies (see Haiman & Knox 1999 for a review), which unfortunately are well below our numerical resolution. Bruscoli et al. (1999) and Gnedin & Jaffe (2000) have modelled reionization using very small-scale high-resolution simulations, probing a range of angular scales complementary to our own, and compute the corresponding microwave anisotropies. We will not consider inhomogeneous reionization in this paper (see Aghanim et al. 1996; Grusinov & Hu 1998; Knox, Scoccimarro & Dodelson 1998; Benson et al. 2000; Valageas et al. 2000), and we will treat the epoch of reionization as an independent parameter. According to Gnedin & Jaffe (2000), anisotropies from inhomogeneous reionization will be subdominant on the scales we consider, especially if massive stars are indeed responsible for reionization.

For the thermal SZ effect the epoch of reionization is irrelevant, as significant signals only come from low redshifts and from regions hot enough to be fully ionized. This is no longer true for the kinetic effect, where the increased density of material at high redshift (per observed solid angle) maintains a significant signal even though the velocities are

smaller. Indeed, we will see that, unlike the thermal SZ signal, the kinetic SZ signal is not convergent and results are mildly dependent on the assumed redshift of reionization (though this is certainly not the largest uncertainty in our calculations). For ease of comparison between cosmologies, we will assume that reionization took place at redshift 10, which satisfies all existing observations (see e.g. Griffiths et al. 1999; Haiman & Knox 1999), independent of the cosmology even though detailed calculations would favour later reionization in the high-density case.

### 2.3 The equations

The thermal SZ effect in a given direction is computed as a line integral, which gives the Compton  $y$ -parameter as (Sunyaev & Zel'dovich 1972, 1980)

$$y = \int \frac{k_B \sigma_T}{m_e c^2} T_e n_e dl. \quad (1)$$

In this expression  $T_e$  and  $n_e$  are the temperature and number density of the electrons,  $k_B$  the Boltzmann constant,  $\sigma_T$  the Thomson cross-section,  $c$  the speed of light and  $m_e$  the electron rest mass. The frequency dependence of the effect is well documented (e.g. Birkinshaw 1999); ignoring relativistic corrections, it gives a temperature fluctuation

$$\frac{\Delta T_{\text{th}}}{T} = y \left[ \frac{x}{\tanh(x/2)} - 4 \right]. \quad (2)$$

where  $x = h\nu/k_B T$  is the dimensionless frequency and  $T$  the radiation temperature. In the long-wavelength limit  $x \ll 1$  (the Rayleigh–Jeans portion of the spectrum) we have  $\Delta T_{\text{th}}/T \simeq -2y$ , and the thermal effect has a null point at  $x \simeq 3.83$ , corresponding to  $\nu \simeq 217$  GHz.

Whenever the gas has a peculiar velocity in the CMB radiation frame, there is a kinematic Doppler effect in addition to heating from the random thermal motions of the electrons. The change in the spectral intensity due to the kinetic effect is (Sunyaev & Zel'dovich 1980)

$$\Delta I_\nu = -I_0 h(x) \frac{v_r}{c} \tau \quad (3)$$

where  $I_0 = 2k_B^3 T^3 / h^2 c^2$ ,  $v_r$  is the line-of-sight velocity of the gas (positive/negative when receding/approaching),  $h(x)$  is given by

$$h(x) = \frac{x^4 e^x}{(e^x - 1)^2}, \quad (4)$$

and  $\tau$  is the optical depth

$$\tau = \int \sigma_T n_e dl. \quad (5)$$

The temperature fluctuation due to the kinetic effect is

$$\frac{\Delta T_k}{T} = -\frac{v_r}{c} \tau = -\int \frac{v_r}{c} \sigma_T n_e dl, \quad (6)$$

which, in contrast to the thermal effect, is a frequency-independent quantity. As such, the kinetic effect cannot be distinguished from primary microwave anisotropies on the basis of its spectral dependence.

### 3 THE MAPS

For full details as to the construction of maps, see da Silva et al. (2000). The starting ingredient is a set of three hydrodynamical simulations, one for each of three cosmologies.

- $\Lambda$ CDM: a low-density model with a flat spatial geometry and  $\Omega_0 = 0.35$  and  $\Omega_\Lambda = 0.65$ .
- $\tau$ CDM: a critical-density model with  $\Omega_0 = 1$  and  $\Omega_\Lambda = 0$ .
- OCDM: a low-density open model with  $\Omega_0 = 0.35$  and  $\Omega_\Lambda = 0$ .

The simulations were carried out using the public domain Hydra code (Adaptive P<sup>3</sup>M-SPH: Couchman, Thomas & Pearce 1995). In each case the box-size was  $150 h^{-1}$  Mpc, and equal numbers of dark matter and gas particles were used.

To construct a map we stack simulation output boxes, with random translations and reorientations, to reach high redshift. Outputs from the simulations were made at different epochs so that they can be stacked smoothly into an evolving sequence. Typically around 35 boxes need to be stacked to reach to redshift 10; however at the redshifts from which the bulk of the signal arises only a small fraction of the volume of the box contributes to the maps and so we are not limited by cosmic variance in having only a single hydrodynamical simulation. For each cosmology we make 30 different maps, corresponding to different random orientations of the stacked simulations.

To compute the thermal and kinetic effects we follow the approach described in da Silva et al. (2000). In the simulations each gas particle occupies a volume with radius proportional to its SPH smoothing radius,  $h_i$ , inside which the mass profile is taken as  $m_{\text{gas}} W(\mathbf{r} - \mathbf{r}_i, h_i)$ , where  $\mathbf{r}_i$  is the position of the particle's centre,  $m_{\text{gas}}$  is the mass of the gas particle and  $W$  is the normalized spherically-symmetric smoothing kernel.

The quantities we are interested in mapping are  $y$  and  $\Delta T_k/T$ . To do this we first convert the line-of-sight integrations in equations (1) and (6) into volume integrals over space. The resulting expressions are then discretized into cubic cells of volume  $V$  (voxels), which are stacked along the line of sight to produce pixels of area  $A$ . The total temperature distortion induced by the kinetic effect in each pixel of the map can then be evaluated as

$$\frac{\Delta T_k}{T} = -\frac{\sigma_T}{c} \frac{V}{A} \frac{0.88 m_{\text{gas}}}{m_p} \sum_i \sum_\alpha v_{r,i} W(|\mathbf{r}_\alpha - \mathbf{r}_i|, h_i), \quad (7)$$

and likewise for the thermal SZ  $y$ -parameter

$$y = \frac{k_B \sigma_T}{m_e c^2} \frac{V}{A} \frac{0.88 m_{\text{gas}}}{m_p} \sum_i \sum_\alpha T_i W(|\mathbf{r}_\alpha - \mathbf{r}_i|, h_i), \quad (8)$$

where the  $i$  index runs over all particles which contribute to the pixel columns, and the  $\alpha$  index is over the line-of-sight cubes. For each particle the sum of the smoothing kernel over voxels is normalized to  $1/V$ . The quantities  $y$  and  $\Delta T_k/T$  are the average values in each pixel. In these expressions,  $v_{r,i}$  and  $T_i$  are the velocity and the temperature of the gas particles,  $m_p$  is the proton mass, and the factor 0.88 gives the number of electrons per baryon, assuming a 24 per cent helium fraction and complete ionization in the regions of in-

terest. We construct maps of the individual simulation boxes in our stacking, which are then added to give the final maps.

### 4 RESULTS

Typical example maps in each cosmology are shown in Figure 1, with the same colour scale in each.\* The original maps have been smoothed using a gaussian with a full-width half-maximum (FWHM) of  $1'$ . Unlike the thermal maps, the kinetic maps show positive and negative temperature fluctuations. The low-density maps (top and bottom panels) present stronger fluctuations than the critical density ones (centre panels). The brightest objects in the thermal maps do not necessarily correspond to the largest kinetic distortions (and vice-versa). However, bright thermal sources often reveal neighboring kinetic peaks of opposite signs (Diaferio, Sunyaev & Nusser 2000), resulting from mergings of substructures or rotational flows within the sources. This can be seen, for example, corresponding to the two brightest objects of the thermal  $\Lambda$ CDM map and in the bright source on the lower right corner of the OCDM map. These objects are at redshifts  $z=1.7$ , 1.8, and 1.9 respectively. Fainter super-clusters at lower redshifts also produce similar signatures (see animations of individual maps on our WWW page), but their contribution to the final map tends to be erased by the box stacking process. Although the kinetic effect has no spectral signature, the search for these characteristic positive/negative features in the SZ flux of bright sources and nearby super-clusters may prove to be an additional aid in isolating the kinetic effect in future SZ measurements and in identifying super-clusters at cosmological distances (see Diaferio et al. 2000).

#### 4.1 The redshift dependence

In order to test how well the calculation of the effects converges with redshift, Figure 2 shows the rms distortion,  $\sigma_k = \sqrt{\langle (\Delta T_k/T)^2 \rangle}$ , in the 1 arcminute resolution maps constructed out to redshift  $z$ , as a function of that redshift. Unlike the dispersion of the thermal effect, shown in Figure 3, the integrated kinetic signal is not strongly convergent to high redshift, with the smaller velocities being compensated by the increased amount of material contributing. In the real Universe the signal is cut off by the epoch of reionization, and as can be seen our results are modestly dependent on that choice (though other uncertainties such as the normalization of the matter power spectrum will be more significant). As advertised in Section 2, we choose to construct maps with data out to redshift 10 in each cosmology.

#### 4.2 The dispersion

In Table 1 we list the rms fluctuations in both the thermal and kinetic effects, for a range of different smoothings to represent possible instrumental resolutions. They are given as

\* A more extensive selection of colour maps, along with animations showing the contribution from each redshift, can be found at [star-www.cpes.susx.ac.uk/~andrew1/sz/sz.html](http://star-www.cpes.susx.ac.uk/~andrew1/sz/sz.html)

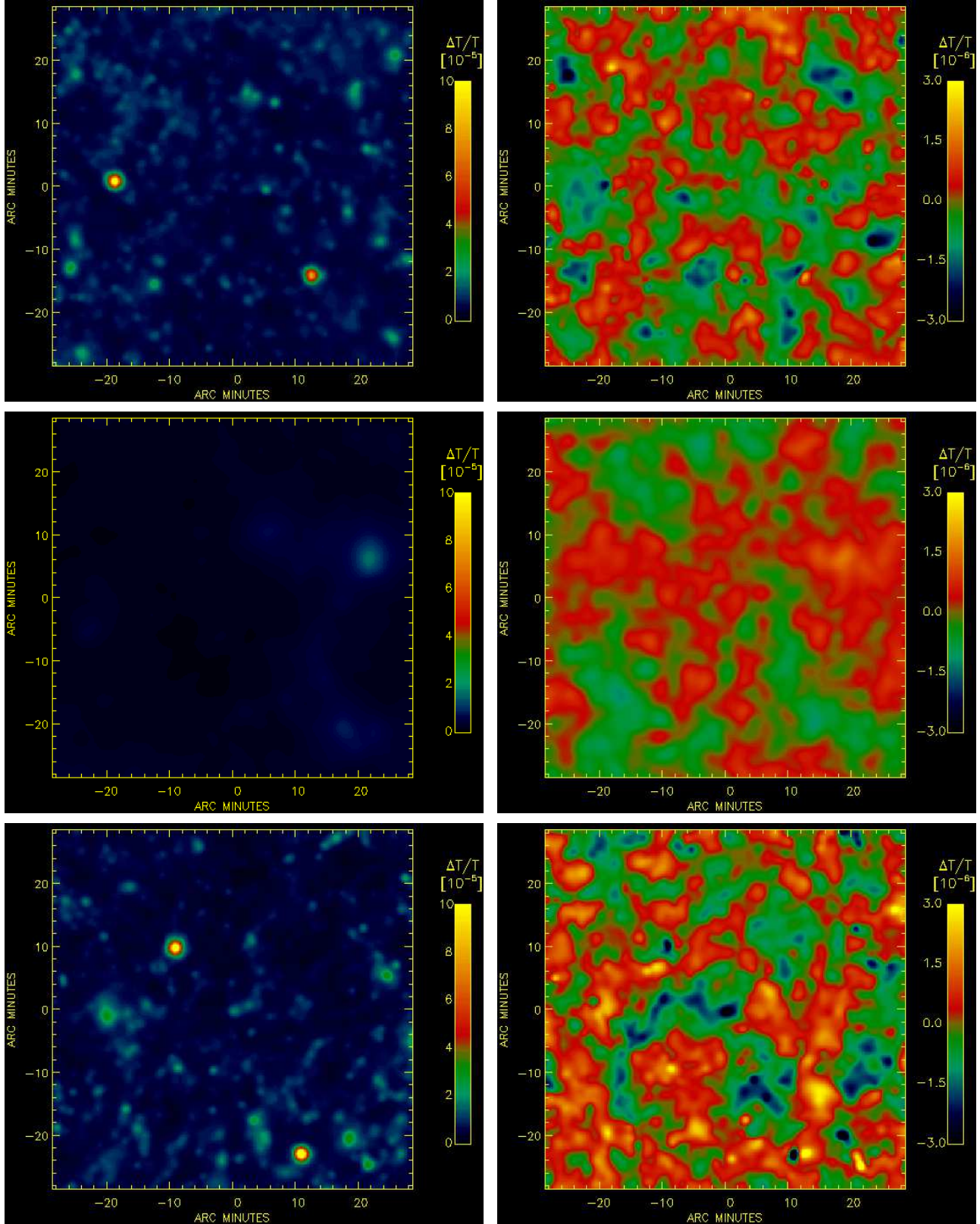


**Figure 1.** Pairs of simulated SZ maps of size one square degree. The left panels show  $\Delta T_{\text{th}}/T$  in the Rayleigh–Jeans part of the spectrum, while the right panels show the corresponding kinetic maps of  $\Delta T_k/T$  from the same map realization. In each case, the original map was convolved with a gaussian beam profile of FWHM = 1'. From top to bottom, the three sets are  $\Lambda$ CDM,  $\tau$ CDM and OCDM.

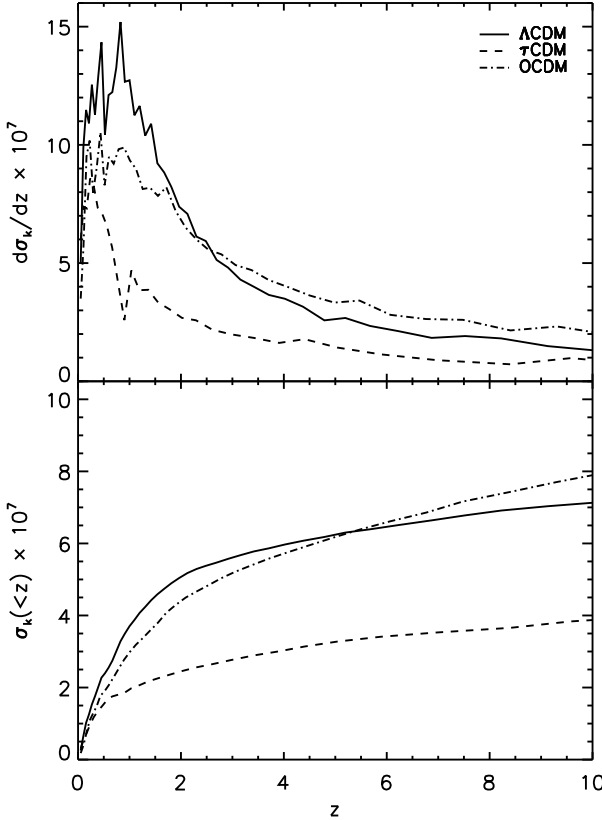


**Figure 2.** The rms kinetic distortion in the  $1'$  resolution maps made from individual simulation boxes at a redshift  $z$  (upper panel), and the rms of the accumulation of these maps up to redshift  $z$  (lower panel). Each curve is an average over the 30 map realizations. Note that the lower panel is not simply the integral of the upper, because when kinetic maps are added together they ‘interfere’.

**Table 1.** The rms fluctuations of the thermal ( $\sigma_{\text{th}}$ ) and kinetic ( $\sigma_k$ ) SZ effects as a function of beam resolution in the Rayleigh-Jeans limit. Values are in multiples of  $10^{-7}$ .

	1'		2'		5'		10'	
	$\sigma_{\text{th}}$	$\sigma_k$	$\sigma_{\text{th}}$	$\sigma_k$	$\sigma_{\text{th}}$	$\sigma_k$	$\sigma_{\text{th}}$	$\sigma_k$
$\Lambda\text{CDM}$	42	7.2	33	6.1	20	4.1	11	2.4
$\tau\text{CDM}$	11	3.8	10	3.5	8.5	2.6	5.9	1.7
OCDM	40	8.0	31	6.7	18	4.4	10	2.5

temperature fluctuations in the long-wavelength part of the spectrum. Because the thermal effect is purely additive, its fluctuations, which is all that most instruments are capable of measuring, do not dominate over the kinetic fluctuations by as large a factor as one would surmise from looking at the total magnitude of the effects.

### 4.3 The pixel distribution

Figure 4 shows a histogram of the pixel distribution in the kinetic maps for the  $\Lambda\text{CDM}$  cosmology. The different curves represent different smoothings ranging from  $0.5'$  to  $10'$ . The curves show the distribution of  $\Delta T_k/T$  values which would

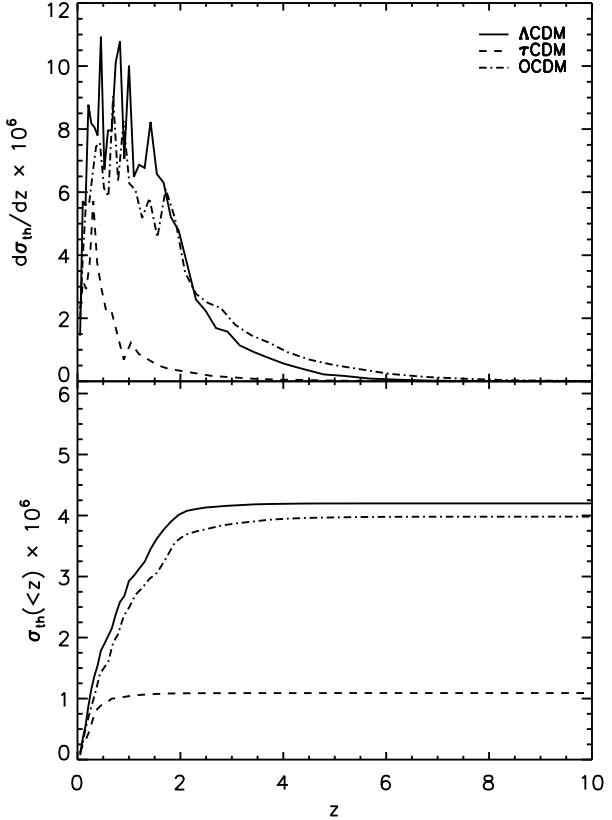


**Figure 3.** As Figure 2 but for the thermal effect. Strong convergence to high redshift is seen. Note that this plot, showing the dispersion, differs from a similar plot in da Silva et al. (2000) which showed the convergence of the mean  $y$ -distortion with redshift.

be seen if an instrument with the corresponding resolution points randomly at the sky. At low resolutions (5 arcminutes or worse) the curves are close to gaussian distributed for all intensities, whereas at higher resolution marked nongaussian tails are present from non-linear structures. These nonlinear tails represent the best hope for observing the effect directly. As expected the pixel distribution mean values are very close to zero.

These pixel distributions are quite discouraging for attempts to detect the kinetic effect from individual sources with the *Planck* satellite, whose best resolution is about five arcminutes. We see that the pixel distribution at such resolution is well approximated by a gaussian even for the rarest events we see, with no non-gaussian tail of bright rare events. The rms dispersion is very small compared to the expected level of primary anisotropies on those scales, and so the kinetic effect will not be detectable directly without some external information as to where to look to see it. Later in this paper, we shall consider the use of the thermal effect as an indicator of where to look for the kinetic effect. This can allow a statistical measure of the cluster velocity field (Aghanim et al. 1997; see also Haehnelt & Tegmark 1996; Hobson et al. 1998). Indeed, the MAP and *Planck* missions could allow the overall detection of the cosmic bulk flow when coupled with X-ray observations (Kashlinsky & Atrio-Barandela 2000).

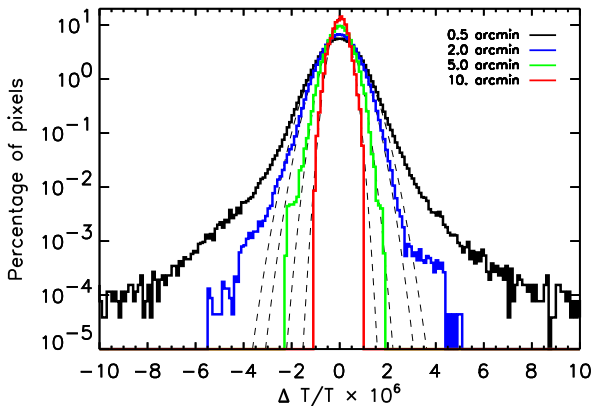


**Figure 4.** A histogram of the  $\Delta T_k/T$  values in the  $\Lambda$ CDM maps with different smoothings. The dashed lines show gaussian fits to the distributions.

#### 4.4 The angular power spectrum

We calculate the power spectrum using the flat-sky approximation in the usual way; see e.g. Peacock (1999). In Figure 5 we show the thermal and kinetic SZ angular power spectra obtained from simulations for the three cosmologies, with the  $C_\ell$  band averaged into logarithmic bins in the Fourier space.

The power spectra shown are averages over the thirty maps we made for each cosmology. To estimate the statistical error we used bootstrap resampling of the thirty maps, which gave a range of estimates indicated at 68 per cent confidence by the dotted lines (note that the map-to-map variations are of course much bigger than the variation in the bootstrap resamples of thirty maps each). For the two low-density cosmologies we see that the statistical errors are small, while for the critical-density thermal case even thirty maps leaves a significant residual error, because the maps tend to be dominated by the presence or absence of single bright features. Unfortunately computer time limitations prevent us increasing the number of maps used to make the estimate, and from running more sets of hydrodynamical simulations to remove possible correlations from using a single set.

From Figure 5 we see that the low-density models present similar shapes and amplitudes for the thermal and kinetic angular power spectra. In the critical-density case both effects produce less power at all scales, which can be explained by there being fewer objects along the line of sight for this model. On large angular scales, the thermal  $C_\ell$  curves typically exceed the kinetic ones by a factor of about 25 for all cosmologies. On smaller scales ( $\ell \gtrsim 2000$ ) the gap between the thermal and kinetic power spectrum increases slowly in the low-density models, whereas in the  $\tau$ CDM model it decreases rapidly as the thermal  $C_\ell$  curve falls with  $\ell$ . This can be understood if we take into account that although the simulations are normalized to give the same abundance of objects at redshift zero, in the low-density models there are SZ sources visible to much higher redshifts. As we will see below, on small angular scales the thermal SZ

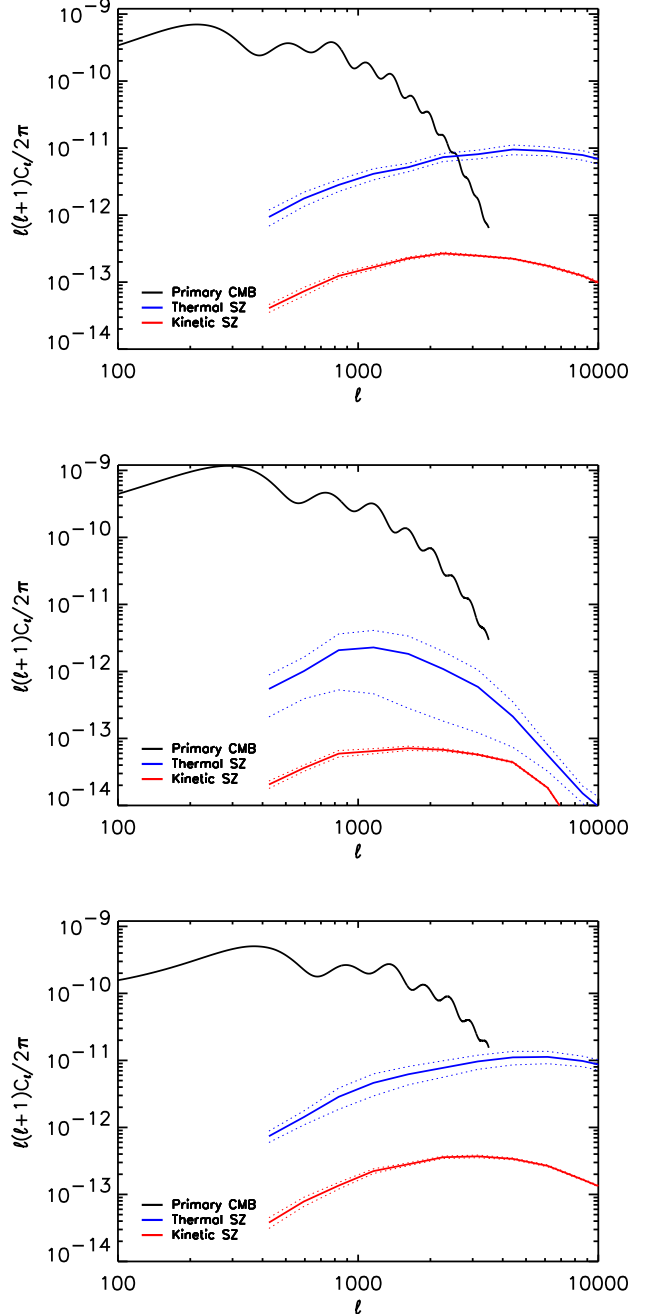


**Figure 5.** In each panel, we see the primary CMB, thermal SZ and kinetic SZ angular power spectra obtained for each cosmology. From top to bottom we have  $\Lambda$ CDM,  $\tau$ CDM and OCDM, respectively. The thermal spectrum is plotted for the Rayleigh-Jeans part of the frequency spectrum, and can be scaled to other frequencies. The dotted lines indicate 1-sigma errors, obtained by bootstrap resampling the thirty map realizations.

spectrum receives strong contributions from sources above redshift one. The lack of distant sources in the  $\tau$ CDM model is then reflected in the thermal SZ power spectrum by a strong reduction of power on these scales.

In the  $\Lambda$ CDM cosmology the amplitude of the thermal SZ power spectrum becomes comparable to the power spec-

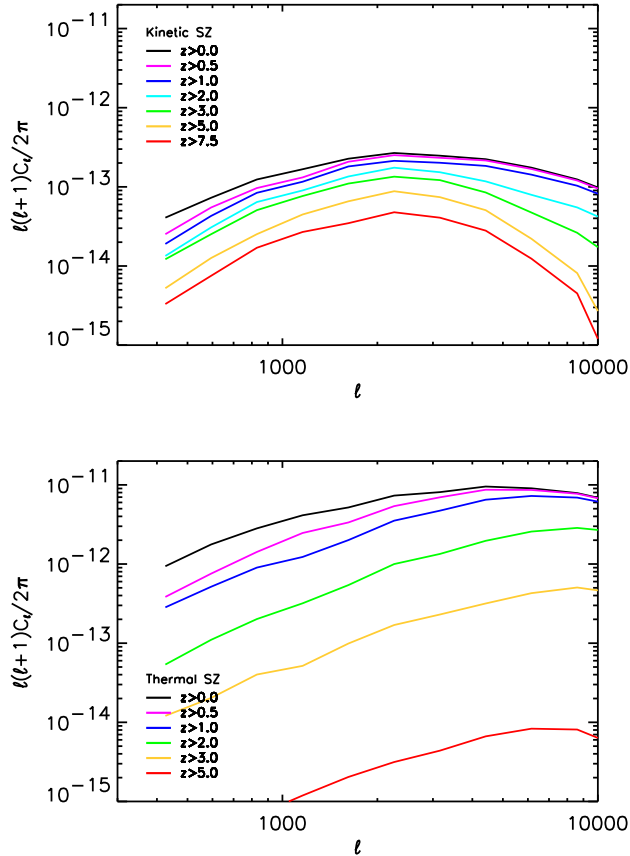


**Figure 6.** The redshift dependence of the power spectrum of the kinetic effect is shown in the upper panel, with the lower panel showing the thermal effect for comparison. In each case, the spectrum is shown for the accumulated signal from redshifts greater than a given value. These plots refer to the  $\Lambda$ CDM simulation.

trum of the primary CMB around  $\ell = 2000$ . This prediction agrees with earlier results from numerical simulations (Refregier et al. 2000a; Seljak et al. 2000; Springel et al. 2000) and confirms that the SZ power spectrum should not be an important source of contamination for MAP (its amplitude is well below the projected noise for this mission, see Refregier et al. 2000a,b), whereas it should be detectable by *Planck* and other experiments probing smaller angular scales.

Figure 6 shows the dependence of the thermal and kinetic angular power spectra with redshift. We see that the kinetic effect has had a much weaker dependence on redshift (for  $\ell \simeq 2000$  about 15 per cent of the power has origin above  $z > 7.5$ ), and indeed, while sub-dominant now, was dominant at redshifts earlier than about three. On large angular scales, the thermal power spectrum is clearly dominated by sources at low redshifts. More than two-thirds of the power on these scales is generated at redshifts  $z < 1$ , whereas on small scales the majority of the signal is produced above redshift 1. On intermediate scales there is still a reasonable fraction of power with origin above  $z = 1$ ; for instance at  $\ell = 2000$  that fraction is about 50 per cent.

In general our results show broad agreement with the SZ power spectra obtained from numerical simulations by

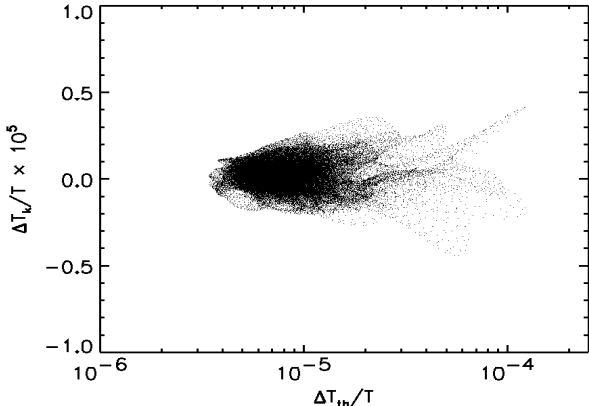


**Figure 7.** A scatter plot of the kinetic effect against the thermal effect, pixel-by-pixel, for a single  $\Lambda$ CDM map.

Refregier et al. (2000a), Seljak et al. (2000) and Springel et al. (2000). In the first two cases the authors have also studied three CDM models, but made no predictions for the kinetic SZ power spectrum. In Springel et al. (2000) the angular power spectrum is computed for both effects, but results are only reported for the  $\Lambda$ CDM cosmology. After taking into account the difference between simulations on  $\sigma_8$  and  $\Omega_B h$  we find that the thermal spectra agree quite well on large angular scales. In particular, our thermal  $\Lambda$ CDM spectrum agrees remarkably well with Springel et al. (2000) for a wide range of  $\ell$  (the difference is within 20 per cent for  $\ell \lesssim 1200$ ). This is an encouraging result as all simulations should agree on these scales (as shown in Refregier et al. 2000a, the finite size of the simulation boxes has very little influence on the SZ power spectrum).

On small angular scales different simulations give rather different results for the thermal effect. Generally speaking our simulations predict less power than Springel et al. (2000) and more power than Refregier et al. (2000a) and Seljak et al. (2000). However, in the critical-density case our thermal curve peaks before and falls faster than the lower limit for the spectrum reported by Refregier et al. (2000a). The fact that Springel et al. (2000) predict more power on these scales is most likely reflecting the higher resolution of their simulations.

The only available results for comparison of the kinetic spectra are those of Springel et al. (2000) for the  $\Lambda$ CDM cosmology. The agreement between simulations is not as good as in the thermal case, as the shapes of the kinetic curves differ on large scales. Our simulations predict about  $\sim 3.5$  times less power at  $\ell \simeq 400$ . However simulations show good agreement in the range  $1000 \lesssim \ell \lesssim 2000$ . Different assumptions concerning the ionization history of the gas may be the main source of differences in the spectra at very high  $\ell$ .

#### 4.5 Kinetic effect versus thermal effect

Given the smallness of the kinetic effect, it is advantageous to have an idea where on the sky to look in order to see it. Such a guide is given by the thermal effect, which indicates locations where gravitational collapse has concentrated scat-

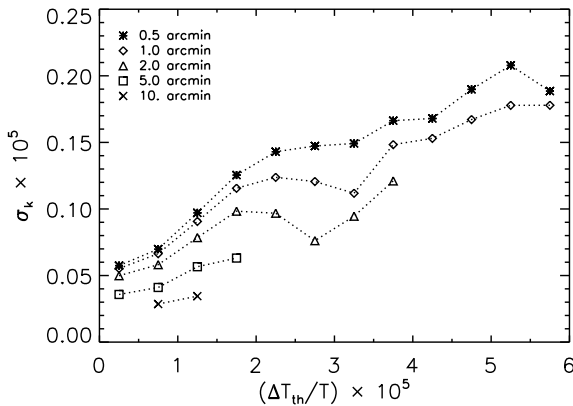


**Figure 8.** For a given value of thermal distortion, this plot shows the dispersion of the values for the kinetic distortion found at the same spatial locations. For the plotted values, the distribution is quite well approximated by a gaussian, whereas for larger values it is dominated by nongaussian effects.

tering electrons. Figure 7 is a pixel-by-pixel scatter plot of the kinetic effect versus the thermal effect, found in a single map of the  $\Lambda$ CDM simulation. The kinetic signal is roughly symmetric around zero and its dispersion increases for the pixels with higher thermal distortions. The ‘tendrils’ are the pixels associated with particular large bright features in the maps.

An interesting question is what values of kinetic distortion are expected at locations with a given thermal distortion, and this is shown in Figure 8. We binned the pixels of all thirty  $\Lambda$ CDM maps according to their thermal values and studied the distribution of kinetic distortions. As long as the distortion is not too large, these distributions are well approximated by gaussians of width  $\sigma_k$  as shown in the figure, the brighter thermal sources corresponding typically to larger kinetic distortions. This enhancement at locations of larger thermal signal is what allows a statistical detection of the magnitude of the kinetic effect (Haehnelt & Tegmark 1996; Aghanim et al. 1997) and may allow detections in some rare bright objects. For a discussion of identifying the kinetic effect through the component separation process, see Hobson et al. (1998).

A similar exercise can be carried out for identified sources rather than pixels. To mimic typical observational procedures, we first subtract the mean signal from the thermal maps. We then identify source locations in the thermal maps using the SExtractor package (Bertin & Arnouts 1996), and determine the total thermal flux of the sources (at a given frequency channel) by adding up the flux in all contiguous pixels until the pixel intensity falls below half the maximum. In order to reduce source confusion effects we only consider bright resolved sources which satisfy the selection criterion of having a half maximum intensity above twice the rms distortion in the maps. We then compute the corresponding flux of the kinetic effect by summing the same set of pixels in the kinetic maps. Figure 9 shows the resulting scatter plot, at frequency 143 GHz, made from all thirty of

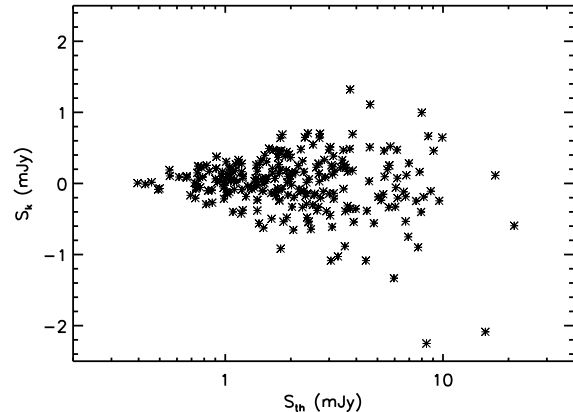


**Figure 9.** As Figure 7, but now showing the total flux of sources as described in text.

the one arcminute resolution  $\Lambda$ CDM maps (unlike the pixel scatter plots which are from a single map).

As expected the largest kinetic distortions correspond to sources with stronger thermal fluxes. However, at this frequency the typical flux of the kinetic effect is around one order of magnitude below the thermal, though for specific clusters the ratio can be as high as one third.

## 5 CONCLUSIONS

We have used hydrodynamical simulations to study a number of aspects of the kinetic SZ effect, including its dependence on cosmological parameters. We have studied the redshift dependence, pixel histograms, angular power spectra, and the correlation between the kinetic and thermal effects. We have confirmed that the kinetic effect has a dispersion more than a factor five below the thermal (in the Rayleigh–Jeans region), leading to an angular power spectrum a factor of typically twenty-five lower in the low-density cosmologies. For critical density we have found a smaller difference, but with much greater statistical uncertainty. For the thermal effect the angular power spectrum is mostly generated at redshifts below one, while for the kinetic effect a significant amount of the power has origin above redshift two. The correlation of the kinetic effect with the thermal confirms and quantifies the expected enhancement of the kinetic effect in regions with a strong thermal signal.

Our simulations are of ideal size to study the SZ effect on scales between one and several arcminutes, which is currently a resolution attracting great interest. Our results complement perfectly the small-scale simulation work of Bruscoli et al. (1999) and Gnedin & Jaffe (2000), and recent semi-analytic work including that of Benson et al. (2000) and Valageas et al. (2000). The theory of these secondary anisotropies is now becoming highly developed; the key challenges for the kinetic effect lie very much on the observational side.

## ACKNOWLEDGMENTS

We are indebted to Hugh Couchman and Frazer Pearce for their part in writing the **Hydra** hydrodynamical *N*-body code used to generate the simulation data used in this work. We thank Jim Bartlett, Julian Borrill, Ian Grivell, Andrew Jaffe, Scott Kay, Alexandre Refregier, Volker Springel, Aprajita Verma and Martin White for helpful discussions and comments. ACdS and DB were supported by FCT (Portugal) and PAT by a PPARC Lecturer Fellowship. We acknowledge use of the Starlink computer systems at Imperial College and at Sussex. The simulations were carried out on the BFG-HPC facility at Sussex funded by HEFCE and SGI, and part of the data analysis on the COSMOS National Cosmology Supercomputer funded by PPARC, HEFCE and SGI.

## REFERENCES

Aghanim N., Désert F.-X., Puget J.-L., Gispert R., 1996, *A&A*, 311, 1

Aghanim N., De Luca A., Bouchet F. R., Gispert R., Puget J.-L., 1997, *A&A*, 325, 9

Atrio-Barandela F., Mücket J. P., 1999, *ApJ*, 515, 465

Barbosa D., Bartlett J. G., Blanchard A., Oukbir J., 1996, *A&A*, 314, 13

Bartlett J. G., Silk J., 1994, *ApJ*, 423, 12

Benson A. J., Nusser A., Sugiyama N., Lacey C. G., 2000, *astro-ph/0002457*

Bertin E., Arnouts S., 1996, *A&AS*, 117, 393, WWW page at [www.eso.org/science/eis/eis\\_doc/sex2/sex2html/](http://www.eso.org/science/eis/eis_doc/sex2/sex2html/)

Birkinshaw M., 1999, *Phys. Rep.*, 310, 98

Bruscoli M., Ferrara A., Fabbri R., Ciardi B., 1999, *astro-ph/9911467*

Carlstrom J. A., Joy M. K., Grego L., Holder G. P., Holzapfel L., Mohr J. J., Patel S., Reese E. D., 2000, *Physica Scripta*, T85, 148

Colafrancesco S., Mazzotta P., Rephaeli Y., Vittorio N., *ApJ*, 1994, 433, 454

Colafrancesco S., Mazzotta P., Rephaeli Y., Vittorio N., 1997, *ApJ*, 488, 566

Cole S., Kaiser N., 1988, *MNRAS*, 233, 637

Cooray A., Hu W., 2000, *ApJ*, 534, 533

Couchman H. M. P., Thomas P. A., Pearce F. R., 1995, *ApJ*, 452, 797

da Silva A., Barbosa D., Liddle A. R., Thomas P. A., 2000, *MNRAS*, 317, 37

Diaferio A., Sunyaev R., Nusser A., 2000, *ApJ*, 533, L71

Eke V. R., Cole S., Frenk C. S., 1996, *MNRAS*, 282, 263

Gnedin N. Y., Jaffe A., 2000, *astro-ph/0008469*

Griffiths L. M., Barbosa D., Liddle A. R., 1999, *MNRAS*, 308, 854

Grusinov A., Hu W., 1998, *ApJ*, 508, 435

Haehnelt M. G., Tegmark M., 1996, *MNRAS*, 279, 545

Haiman Z., Knox L., 1999, *astro-ph/9902311*

Hernández-Monteagudo C., Atrio-Barandela F., Mücket J. P., 2000, *ApJ*, L528, 69

Hobson M. P., Jones A. W., Lasenby A. N., Bouchet F. R., 1998, *MNRAS*, 300, 1

Hu W., 2000, *ApJ*, 529, 12

Jones M. et al., 1993, *Nature* 365, 320

Kashlinsky A., Atrio-Barandela F., 2000, *ApJ*, 536L, 67

Knox L., Scoccimarro R., Dodelson S., 1998, *Phys. Rev. Lett.*, 81, 2004

Komatsu E., Kitayama T., 1999, *ApJ*, 526, L1

Molnar S. M., Birkinshaw M., 2000, *ApJ*, 537, 542

Myers S. T., Baker J. E., Readhead S. A. G., Leitch E. M., Herbig T., 1997, *ApJ*, 485, 1

Ostriker J. P., Vishniac E. T., 1986, *ApJ*, 306, L51

Peacock J. A., 1999, *Cosmological Physics*, Cambridge University Press

Press W. H., Schechter P., 1974, *ApJ*, 187, 425

Refregier A., Komatsu E., Spergel D., Pen U.-L., 2000a, *Phys. Rev. D*, 61, 123001

Refregier A., Spergel D., Herbig T., 2000b, *ApJ* 531, 31

Rephaeli Y., 1995, *ARA&A*, 33, 541

Seljak U., Zaldarriaga M., 1996, *ApJ*, 469, 1

Seljak U., Burwell J., Pen U.-L., 2000, *astro-ph/0001120*

Springel V., White M., Hernquist L., 2000, *astro-ph/0008133*

Sunyaev R. A., Zel'dovich Ya. B., 1972, *Comm. Astrophys. Space Phys.*, 4, 173

Sunyaev R. A., Zel'dovich Ya. B., 1980, *ARA&A*, 18, 537

Valageas P., Balbi A., Silk J., 2000, *astro-ph/0009040*

This paper has been produced using the Royal Astronomical Society/Blackwell Science L<sup>A</sup>T<sub>E</sub>X style file.